Journal of
Composites Science

MDPI

Article

Can Empirical Biplots Predict High Entropy Oxide Phases?

Zhaoyuan Leong [1,*], Pratik Desai [2] and Nicola Morley [1]

[1] Department of Materials Science and Engineering, University of Sheffield, Sheffield S1 3JD, UK; n.a.morley@sheffield.ac.uk
[2] Perlemax Limited, Sheffield S3 7HQ, UK; pratik@perlemax.com
* Correspondence: z.leong@sheffield.ac.uk

Abstract: High entropy oxides are entropy-stabilised oxides that adopt specific disordered structures due to entropy stabilisation. They are a new class of materials that utilises the high-entropy concept first discovered in metallic alloys. They can have interesting properties due to the interactions at the electronic level and can be combined with other materials to make composite structures. The design of new meta-materials that utilise this concept to solve real-world problems may be a possibility but further understanding of how their phase stabilisation is required. In this work, biplots of the composition's mean electronegativity are plotted against the electron-per-atom ratio of the compounds. The test dataset accuracy in the resulting biplots improves from 78% to 100% when using atomic-number-per-atom *Z/a* ratios as a biplot parameter. Phase stability maps were constructed using a Voronoi tessellation. This can be of use in determining stability at composite material interfaces.

Keywords: high entropy oxides; semi empirical design; metamaterials; phase stability

Citation: Leong, Z.; Desai, P.; Morley, N. Can Empirical Biplots Predict High Entropy Oxide Phases? *J. Compos. Sci.* **2021**, *5*, 311. https://doi.org/10.3390/jcs5120311

Academic Editor: Francesco Tornabene

Received: 24 September 2021
Accepted: 18 November 2021
Published: 26 November 2021

1. Introduction

Redox-active metal oxide/carbon composites can play a crucial role in upcoming technologies of energy conversion and energy storage especially in areas such as batteries and water electrolysis [1–3]. The development of cost-efficient oxygen evolution reaction electrocatalysts based on low-cost 3d transition metals oxides is a priority challenge of materials chemistry. A variety of properties are associated with these materials such as the requirement for lower overpotentials, long operational times, and chemical stability under very oxidative and corrosive conditions.

The demand for energy storage devices in stationary and mobile applications has increased rapidly over the past years and will continuously increase in the future. Commonly used electrochemical energy storage devices are intercalation-based Li-ion batteries with high efficiency and reversibility. There is a push to achieve higher energy storage capacity in systems. Li-ion batteries present several problems throughout the production, distribution, utilisation, and disposal process.

A new class of oxide systems known as high-entropy oxides (HEO) was recently reported [4–6]. These materials are based on the concept of entropy stabilisation, where the large number of cation additions (typically >5) can stabilise relatively simple single-phase structures (i.e., rock-salt, fluorite, or perovskite). Due to the electronic interactions between the cations, these compounds can show interesting properties [6–8]. Research in high-entropy oxides is driven by the possible potential to obtain novel properties by exploiting the high-entropy concept and thereby the various electronic interactions that occur during the combination of various cations.

Transition metal oxide (TMO) anode-based batteries have better storage capacities (500–1000 $mAhg^{-1}$) compared to more common graphite anodes (372 $mAhg^{-1}$). This is because the magnetic behaviour of TMOs lead to a strong surface capacitance[1]. However, conventional TMOs show rapid capacity drops due to crystal structural changes from

volumetric changes during cycling. Whereas HEOs have more stable crystal structures while achieving high storage capacities (~920 $mAhg^{-1}$) due to entropy stabilisation. As many HEO properties are tied to its structure, understanding the structural stability of HEOs is a key step towards optimising and designing functional HEO properties.

The high-entropy concept was first reported for metallic systems where they are known as high-entropy alloys (HEA), which leads to the stabilisation of simply solid solutions (i.e., FCC, BCC, and HCP) [9,10]. In the HEA field the design of HEAs can take two routes: through data-driven discovery (DDD) and functionality-driven discovery (FDD). In DDD a database of properties is collected for tested material compositions and targeted properties can be achieved through interpolation of the available composition with respect to required properties. Data from exploratory and characterisation frameworks can be represented in Ashby-diagram property maps or the equivalent for this purpose. In principle, the number of available elements severely reduces the efficacy of this approach. Consider a compound with five alloying additions that are to be picked from 20 elements: here 15,504 possible equimolar combinations are possible.

In FDD materials are developed with targeted properties using search and optimisation strategies. Prediction models (i.e., ab-initio or other semi-empirical models) are used in conjunction with FDD to determine the microscopic parameters that govern material properties. FDD is useful in exploring design candidates in materials with high degree-of-freedoms such as high-entropy systems as extrapolation from experimental data is not necessarily a good predictor of quantum mechanical behaviour. These models can then be used to iterate over many stoichiometries using metaheuristic strategies to determine material compositions of interest. Although the gold-standard for material predictions lie with ab-initio methods, applying reasonably accurate lower-fidelity semi-empirical models can function as a first pass method for identifying potentially useful compositions that may be studied in-depth in combination with ab-initio methods.

Oxide materials can be used as components for composites materials to optimise their properties. In HEOs, examples are $(FeCoCrMnZn)_3O_4$/nickel foam [11], $La_{0.8}Sr_{0.2}MnO_3$-$Ce_{0.8}Sm_{0.2}O_2$ [12], and metal oxide-carbon composites [13]. When different components are brought together to form a composite, their electronic interactions can lead to unexpected behaviour. Examples are charge transfer, strain, symmetry breaking, electrostatic coupling, etc. These properties can be linked to phase transitions and phase stabilities. It is thus important to understand not only how elemental additions during the synthesis process can affect phase stability, but whether ionic migration at the composite interface will affect phase stability.

In HEO design the enthalpy of mixing and the configurational entropy are considered important parameters denoting the formation of a stable phase. Additionally, elemental selection requires selection of cation size to accommodate the oxygen sub-lattice, and valency of the cation additions are selected to maintain the charge balance [14]. These properties are analogous to those found in HEA design where the atomic size mismatch, enthalpy of mixing, configurational entropy, and valence electron concentration are all important parameters for design. These parameters have been developed into semi-empirical models that can be used in FDD [15–17], and due to the similarities between HEO and high-entropy alloys it may be that such models could be useful in HEO design.

In this work we will test this hypothesis by investigating semi-empirical parameter biplots to determine if phase stability can be predicted using these values.

2. Parameter Selection for Phase Stability

High-entropy alloys phase stability predictions use a combination of the Hume-Rothery rules for alloying together with thermodynamic parameters as empirical guidelines. In Dominguez et al.'s work [15], principal component analysis was used to study the contribution of five parameters (electronegativity difference, enthalpy of mixing, entropy of mixing, atomic size difference, and valence electron concentration). These parameters are analogous to those used in HEO design where the valence electron concentration

and electronegativity difference describes charge transfer characteristics. Leong et al. [16] demonstrated that the mean electronegativity of the biplots can be used to determine the phase stability of HEAs when used together in biplots with enthalpy of mixing values, and studies have been shown that electronegativity (X) values can be used to design oxides for use as supercapacitors [18].

In HEAs, the Mulliken and Allen electronegativity scales were found to offer the best separation between structures when presented in a biplot against the enthalpy of mixing when compared to valence electron concentration and the Pauling electronegativity scale. This is attributed to the derivation of the various electronegativity scales: the Mulliken electron negativity is an absolute scale that is derived from the average of the ionisation potential and electron affinity [19] while the Allen electronegativity is derived from the average one-electron energy of the s and p valence-shell electrons in a ground-state free atom [20]. In contrast, the Pauling scale [21] is derived from heats of formation and combustion of gaseous molecules. This derivation affects its effectiveness in making semi-empirical predictions since the reactivity of gaseous compounds can be vastly different from their solid and liquid forms due to significantly higher entropy and kinetic energy for collisions. For the valence electron concentration (VEC), the enthalpy of mixing scales linearly with it with some deviations due to incorrect quantum behaviours being represented [16,22]. The origin of the biplot's ability to differentiate changes in the local environments can be written as [16]:

$$\Delta H = f_{Total}(\overline{n})\Delta n^2 \approx k_2.\overline{n} \quad (1)$$

where $\overline{n}$ is the average band filling represented by the average number of d-electrons, Δn^2 is the difference in the number of valence d-electrons squared [23], $f_{Total}(\overline{n})$ is the sum of the attractive and repulsive contributions, and k_2 is a material constant that is related to the change in energy of the electronic structure upon alloying. k_2 is thus reliant on the deviations between rule-of-mixtures electronegativity values (assuming equal charge redistribution), and the formation of highly-covalent bonds, which leads to a non-linear change in the charge redistribution. It is the magnitude of this error that allows the prediction and separation of phases in the ΔH-X biplots. Thus, without the influence of electronegativity, ΔH scales almost linearly with VEC.

Utilising this concept for HEOs presents some challenges. First, Miedema's enthalpies of mixing [24] which was expanded by Takeuchi and Inoue for use in their sub-regular solid solution to predict bulk metallic glass stabilities [25–27] is used to represent the mixing in metallic compounds. The bonding nature of metallic compounds are somewhere between an ionic and a covalent bond–the degree of this fluctuates and is dependent on the degree of charge transfer resulting from electronic interactions. In metal oxides, the covalent-type bonds dominate, which may make the enthalpy of mixing unsuitable for predictions. Dahlborg et al. have reported on the use the reduced VEC: the electron *per* atom ratio, e/a [28]. However, both the e/a ratio and VEC used for HEAs do not account for size effects which can affect oxide structure more than in metals. As a result, a similar parameterisation of the atomic number, Z is considered. The calculations here will also use the atomic number per atom (Z/a) ratio. Furthermore, oxide bond formation can also proceed through the formation of ligands; in the case of metal oxides the d-orbitals play a critical role in bond formation. Thus, the valence d-electrons can also be considered as a prediction parameter.

Ghosh developed a new electronegativity [29] that was verified with the bond energies of a number of compounds based on the polarizability of the elements. They reported good comparison with a number of oxides, ionic bonded compounds, transition metals, and inert gases. Previous work [16] has shown that the biplots do not accurately account for alloys with elemental additions possessing disparate primary quantum numbers (i.e., different periods). In contrast to the other two compared here the Ghosh electronegativity demonstrates the capability to distinguish between the primary quantum numbers of the individual elements.

As such, we hypothesise that X_{Ghosh} will be able to distinguish between phase stabilities of HEOs. VEC, *Z/a* and valence *d*-electrons will be investigated as potential parameters for biplot differentiation, and two other electronegativity scales (Pauling and Mulliken) will also be investigated to test the hypothesis.

3. Method and Calculation

The dataset used in this study consists of 165 HEO compositions selected from the literature. The compositions in the dataset are a good mix of compositions synthesised using different methodologies and a full list of the compounds may be found in the Supporting Information. The compositions have been initially differentiated according to the phase they display (single and mixed phases). The single phases have then been further categorised into the following phases: Monoclinic, Pyrochlore, Spinel, Fluorite, Rock Salt, Perovskite, and Others. The other phases consist of Bixbyite, Garnet, Rutile, and Magnetoplumbite phases due to the low sample size (1 each or so). Table 1 below demonstrates these subdivisions.

Table 1. Total number of alloy compositions analysed for this study. The dataset has been subdivided into several groups as shown below.

General Grouping	Phase Grouping	No. of Compositions
Mixed	Various	11
Single	Monoclinic	4
	Pyrochlore	18
	Spinel	25
	Fluorite	25
	Rock salt	40
	Perovskite (Ortho)	18
	Perovskite (Cubic)	15
	Others	5

The *Z/a*, VEC, *d*-electron and electronegativity values of these elements are obtained from the values of each oxide's constituent elements. The parameters are combined according to their stoichiometric fraction to obtain the averaged value of a particular compound. By taking the biplot of *Z/a* against the electronegativity we will determine the efficacy of the biplot in determining phase stability.

To aid in distinguishing the relevant areas that represent zone of phase stability, the biplot will be analysed by using a cluster-analysis based approach. The centre-of-balance of each phase grouping can be determined by minimising the Euclidean *distance* between the centre position with respect to the other points:

$$distance(x, y) = \sum_i \sqrt{\delta x_i{}^2 + \delta y_i{}^2} \quad (2)$$

This point is defined as the cluster centre and an ellipsoid can be fitted around this cluster centre so that the ellipse skew and radii is fitted based on the standard deviation of the points. This fitting is accomplished using an algorithm and so minimises the chance of experimenter bias in selecting bounding regions. Any errors, if present, can be attributed to a standard error whose contribution is determined by the programming of the algorithm. The Mathematica [30] program contains the Multivariate Statistics package that fits an Ellipsoidal quantile for bivariate data which is useful for analysis the biplots used in this work. This EllipsoidQuantile function will be used to analyse the results of the biplot; the quantiles selected will follow the three-sigma rule-of-thumb to determine fitting ellipsoids.

4. Results and Discussion

For each composition listed in Supplementary Materials B (for breakdown of types cf. Table S1), the rules-of-mixtures was used to calculate the Ghosh electronegativity, Mulliken electronegativity, Pauling electronegativity, valence electron concentration, d-valence, and atomic number per atom. These 6 parameters combine together to form a 3^2 design-of-experiment grid for 9 possible combinations, which were analysed using the method outlined above (cf. Equation (1)). Each biplot can be found in the Supplementary Materials. The degree of overlap was computed within 2-sigma accuracy (95% of points within the bounding circle) and the total degree of overlap is presented in Table 2 below where it can be observed that the *d*-valence/X_{Ghosh} plot possessed the least amount of overlap variation. The *d*-valence/X_{Ghosh} plot will be discussed below–the other plots can be found in the Supplementary Materials.

Table 2. Cluster overlap values for a 3^2 design-of-experiment grid of three electronegativity values (Ghosh, Mulliken, and Pauling) and three atomic parameters: *d*-valence, valence electron concentration (VEC), and atomic number per atom (*Z*/*a*).

Overlap	X_{Ghosh}	$X_{Mulliken}$	$X_{Pauling}$
d-valence	18.11	19.43	19.01
VEC	33.38	38.76	38.38
Z/*a*	93.08	93.33	93.55

Figure 1a shows the biplot for the *d*-valence scale plotted against X_{Ghosh}. Each group of compounds occupy roughly the same space in each of the biplot regions (cf. Supplementary Materials) for each given value on the *x*-axis (i.e., *d*-valence, VEC, or *Z*/*a*). Each group is encapsulated by three ellipsoids that represent (moving outwards) a 66% (1 sigma), 92% (2 sigma), and 97% (3 sigma) approximate fitting accuracy respectively.

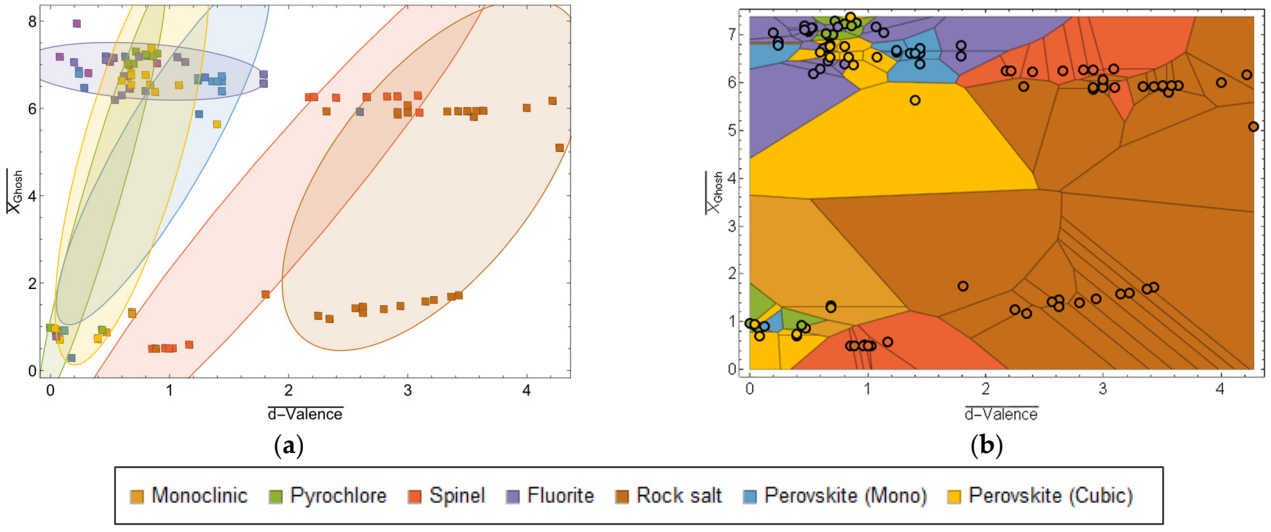

Figure 1. Biplots of HEO compositions as (**a**) *d*-valence vs. X_{Ghosh}, (**b**) the Voronoi tessellation of *d*-valence vs. $X_{Mulliken}$.

Spinel and rock salt structures in the biplots experience significant overlap when compared to the other structures. This may be due to the fact that both are cubic close-packed structures with cations distributed over various octahedral and tetrahedral sites. The spinel to rock salt transformations has been previously reported to occur in oxides which is driven by cation separation instead of a topotactic phase transformation [31]. This appears to parallel the formation of secondary structures in HEAs which is driven by chemical reordering during spinodal decomposition. It may be that HEOs can be

tuned to display similar behaviour for compositions that lie in the interface between stability regions.

There is similarly significant overlap between the Pyrochlore, Fluorite, and both Perovskite groups (Monoclinic and Cubic). This group of structures have an underlying face-centre cubic motif of the parent lattice with different site occupancies within the lattice itself. There are similarly reports in the literature of transitions between these phases (e.g., perovskite to fluorite).

The degree of overlap between each phase means that a strategy to differentiate between regions of phase stability is needed. One simplistic way to do this is to use a Voronoi tessellation, where a point is partitioned into a particular area so that the bounding region is equidistant between the points. This analysis has been performed for the X_{Ghosh}-*d*-valence biplot in Figure 1a and the results are shown in Figure 1b. The results in Figure 1b generally show good continuous partitioning between the phases in the biplot. Other plots are shown in the Supplementary Materials. There is a dearth of points for values between $2 < X_{Ghosh} < 5$. These values in general correspond to X_{Ghosh} values of the metallic elements which demonstrate some degree of metallic bonding. The overlap region containing the Pyrochlore, Fluorite, and both Perovskite phases are now distinguished in the plot.

For example, $A_2B_2O_7$-type compositions predominantly display the perovskite or pyrochlore structure. As a rule of thumb, pyrochlore-stable structures display smaller A/B radius ratios ($Eu_2Ti_2O_7$, $Lu_2Ti_2O_7$ and $Y_2Ti_2O_7$) while perovskite structures have larger A/B radius ratios ($La_2Ti_2O_7$, $Pr_2Ti_2O_7$ and $Nd_2Ti_2O_7$) (the origin of the phase change from pyrochlore to perovskite-like layered structure and a new lead-free ferroelectric) [32]. The pyrochlore-stable cations Eu, Lu, and Y (X_{Ghosh}: 5.0, 6.2, and 3.4) have larger electronegativity values than La, Pr, and Nd (X_{Ghosh}: 4.52, 4.64, and 4.72); this is reflected in Figure 1b where the Pyrochlore cluster is located at the coordinates X_{Ghosh}: 7.22 which is above both Perovskite structures. These plots have the potential to offer further insight in understanding what drives phase change in oxide materials through correlation with mechanism such as ligand formation and electron transfer.

In order to test the efficacy of the prediction scheme, several HEO compositions that have been investigated for their use as battery anodes in the literature. These compositions were not included in the 165-composition dataset use for the analysis above. These compositions are $((Co_{0.2}Cu_{0.2}Mg_{0.2}Ni_{0.2}Zn_{0.2})O$ [33], $(Mg_{0.2}Ti_{0.2}Zn_{0.2}Cu_{0.2}Fe_{0.2})_3O_4$ [34], $((Bi, Na)_{0.2}(La, Li)_{0.2}(Ce, K)_{0.2}Ca_{0.2}Sr_{0.2})$ TiO_3, $(FeCoNiCrMn)_3O_4$ [35], $(MgCoNiZn)_{0.65}Li_{0.35}O$ [36], and $Li_{1.3}Mn_{0.4}Ti_{0.3}O_{1.7}F_{0.3}$ [37]). Non-high-entropy compositions LiF [38], $BaTiO_3$ [39], and $ZnTiO_3$ [39] were also included into the testing dataset to determine prediction accuracy.

Figure 2a–c shows the test dataset overlaid onto X_{Ghosh} biplots as red squares. The points are labeled with their compositions with callout labels and all three predictions are summarized in Figure 2d and compared with the literature experimental values. All three non-high-entropy oxides show good accuracy of predictions within the scheme presented here, highlighting that the methodology described here can be possibly used for regular oxides as well (or including them into an analysis dataset). A 78% accuracy was found to be the case when using the *d*-electron-X_{Ghosh} biplot for fluorite-containing compositions. This demonstrates the failure of the biplot for elements that do not contain d-orbitals. All other compositions are predicted accurately. In contrast when using the Z/a-X_{Ghosh} biplot the accuracy increases to 100%. This is interesting as the earlier overlap analysis suggests significant overlap for the Z/a parameter. This shows that structural stability has many components to it and that simplistic methods such as Euclidean-distance cluster analysis is not sufficient to tease out its intricacies. In comparison, phase stability regions obtained through Voronoi tessellation using hypothesis-based material descriptors are shown here to possess good accuracy.

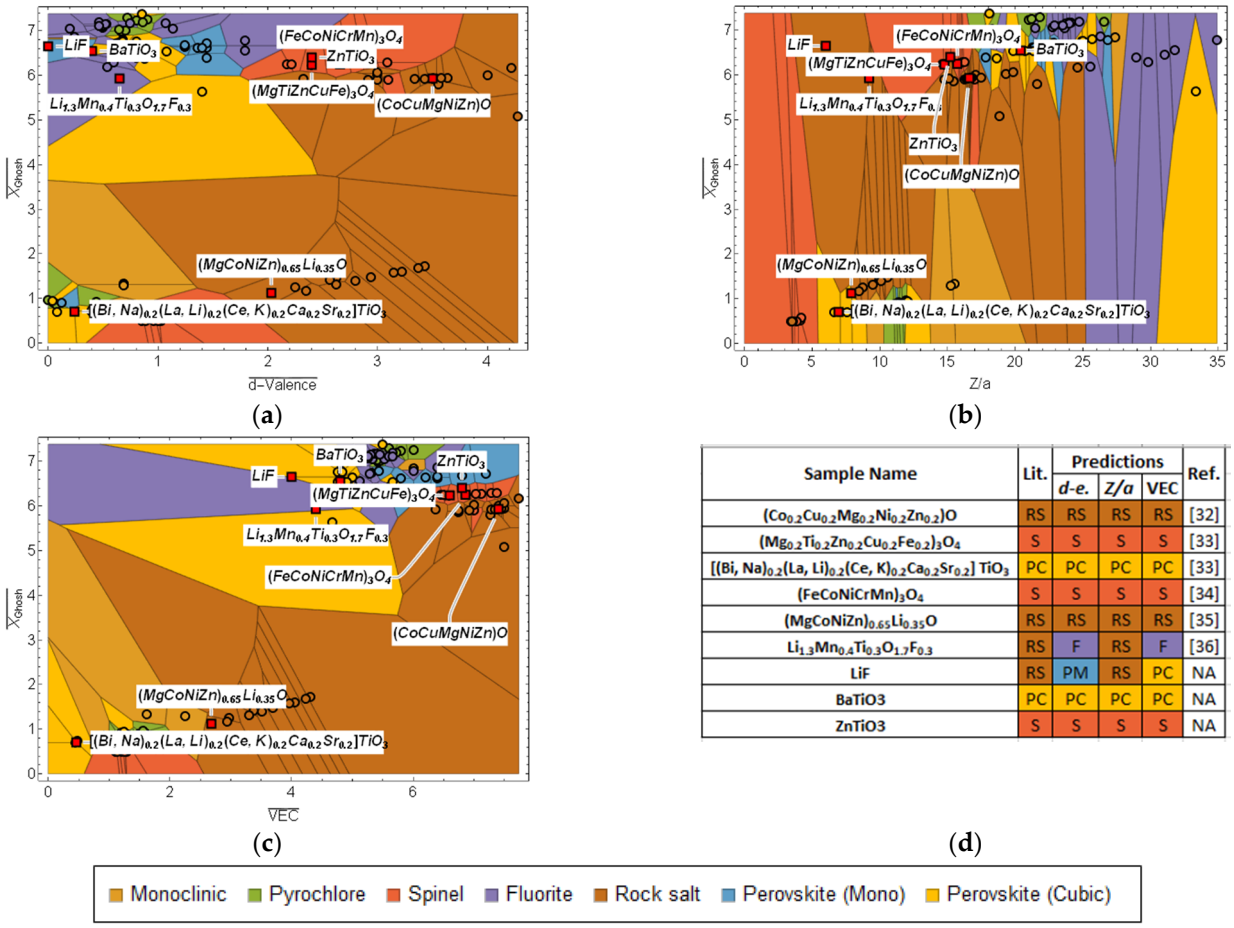

Sample Name	Lit.	Predictions			Ref.
		d-e.	*Z/a*	VEC	
$(Co_{0.2}Cu_{0.2}Mg_{0.2}Ni_{0.2}Zn_{0.2})O$	RS	RS	RS	RS	[32]
$(Mg_{0.2}Ti_{0.2}Zn_{0.2}Cu_{0.2}Fe_{0.2})_3O_4$	S	S	S	S	[33]
$[(Bi, Na)_{0.2}(La, Li)_{0.2}(Ce, K)_{0.2}Ca_{0.2}Sr_{0.2}]$ TiO_3	PC	PC	PC	PC	[33]
$(FeCoNiCrMn)_3O_4$	S	S	S	S	[34]
$(MgCoNiZn)_{0.65}Li_{0.35}O$	RS	RS	RS	RS	[35]
$Li_{1.3}Mn_{0.4}Ti_{0.3}O_{1.7}F_{0.3}$	RS	F	RS	F	[36]
LiF	RS	PM	RS	PC	NA
BaTiO3	PC	PC	PC	PC	NA
ZnTiO3	S	S	S	S	NA

Figure 2. Phase stability regions obtained through Voronoi tessellation for biplots with test dataset predictions overlaid (**a**) *d*-valence vs. X_{Ghosh}, (**b**) *Z/a* vs. X_{Ghosh}, (**c**) *VEC* vs. X_{Ghosh}, and (**d**). Tabulated Prediction of HEO and non-high-entropy metal oxide compositions for three different X_{Ghosh} biplots (*d*-electron, *Z/a*, and VEC.).

5. Conclusions

Biplots of average electronegativity show against the atomic-number-to-atom ratio, *Z/a* can be used to display a discrete phase-composition map for high entropy oxides. This can be used to guide the development of novel HEO compositions that can be incorporated into composite structures for new technologies such as battery anodes. As (1): the crystal structure stability can provide an early idea of the material properties (e.g., oxygen vacancy mobilities changing ionic conduction, redox stability) and (2) phase stability can change in the dealloying fabrication of metal oxide nanocomposites, this methodology can provide a quick way to assess HEO viability. An improvement in predictive capability from 78% accuracy to 100% accuracy was obtained by using *Z/a* parameter in biplots compared to *d*-electron or VEC. The method can be used in a simple algorithm to predict phase stabilities. This can be used to explore interface effects for novel composite oxides.

Supplementary Materials: The following are available online at https://www.mdpi.com/article/10.3390/jcs5120311/s1, Figure S1: Biplots and encapsulating regions for 32 biplots of rules-of-mixtures Ghosh, Pauling, and Mulliken electronegativities plotted against rules-of-mixtures semi-empirical parameters number of valence d electrons (d¬-valence), atomic number per atom ratio (Z/a), and valence electron concentration (VEC), Figure S2: Biplots and Voronoi Tesselations for 32 biplots of rules-of-mixtures Ghosh, Pauling, and Mulliken electronegativities plotted against rules-of-mixtures semi-empirical parameters number of valence d electrons (d¬-valence), atomic number per atom ratio (Z/a), and valence electron concentration (VEC), Figure S3: Overlay of Z/a-XGhosh biplot with phase stable regions obtained through Voronoi tessellation shown. ((NiCoMgCuZn)(Tix)On values (x: 0, 0.2, 0.4, 0.6, 0.8, and 1.0) are overplotted in the figure, Table S1: Molar ratios of

((NiCoMgCuZn)(Tix)On values (x: 0, 0.2, 0.4, 0.6, 0.8, and 1.0), Table S2: Rules-of-mixtures calculations of ((NiCoMgCuZn)(Tix)On values (x: 0, 0.2, 0.4, 0.6, 0.8, and 1.0) for atomic number per atom (Z/a) and Ghosh electronegativity (XGhosh), Table S3: List of Compositions used for analysis.

Author Contributions: Conceptualization, Z.L. and P.D.; methodology, Z.L.; software, Z.L.; validation, Z.L.; formal analysis, Z.L.; investigation, Z.L.; resources, Z.L.; data curation, Z.L.; writing—original draft preparation, Z.L.; writing—review and editing, Z.L., P.D. and N.M.; visualization, Z.L.; supervision, P.D. and N.M.; project administration, Z.L.; funding acquisition, Z.L. and N.M. All authors have read and agreed to the published version of the manuscript.

Funding: This work is in part funded by the University of Sheffield Engineering Researchers Society Development Opportunities Fund and the Ironmonger's Company Summer Project funding.

Institutional Review Board Statement: Not Applicable.

Informed Consent Statement: Not Applicable.

Data Availability Statement: Data is contained within Supplementary Materials.

Conflicts of Interest: The authors declare no conflict of interest.

References

1. Nitta, N.; Wu, F.; Lee, J.T.; Yushin, G. Li-Ion Battery Materials: Present and Future. *Mater. Today* **2015**, *18*, 252–264. [CrossRef]
2. Reddy, M.A.; Breitung, B.; Chakravadhanula, V.S.K.; Wall, C.; Engel, M.; Kübel, C.; Powell, A.K.; Hahn, H.; Fichtner, M. CFx Derived Carbon-FeF $_2$ Nanocomposites for Reversible Lithium Storage. *Adv. Energy Mater.* **2013**, *3*, 308–313. [CrossRef]
3. Mizushima, K.; Jones, P.C.; Wiseman, P.J.; Goodenough, J.B. LixCoO$_2$ (0< x < −1): A New Cathode Material for Batteries of High Energy Density. *Mater. Res. Bull.* **1980**, *15*, 783–789. [CrossRef]
4. Rost, C.M.; Sachet, E.; Borman, T.; Moballegh, A.; Dickey, E.C.; Hou, D.; Jones, J.L.; Curtarolo, S.; Maria, J.-P. Entropy-Stabilized Oxides. *Nat. Commun.* **2015**, *6*, 8485. [CrossRef] [PubMed]
5. Sarkar, A.; Djenadic, R.; Usharani, N.J.; Sanghvi, K.P.; Chakravadhanula, V.S.K.; Gandhi, A.S.; Hahn, H.; Bhattacharya, S.S. Nanocrystalline Multicomponent Entropy Stabilised Transition Metal Oxides. *J. Eur. Ceram. Soc.* **2017**, *37*, 747–754. [CrossRef]
6. Bérardan, D.; Franger, S.; Meena, A.K.; Dragoe, N. Room Temperature Lithium Superionic Conductivity in High Entropy Oxides. *J. Mater. Chem. A* **2016**, *4*, 9536–9541. [CrossRef]
7. Bérardan, D.; Franger, S.; Dragoe, D.; Meena, A.K.; Dragoe, N. Colossal Dielectric Constant in High Entropy Oxides. *Phys. Status Solidi Rapid Res. Lett.* **2016**, *10*, 328–333. [CrossRef]
8. Sarkar, A.; Loho, C.; Velasco, L.; Thomas, T.; Bhattacharya, S.S.; Hahn, H.; Djenadic, R. Multicomponent Equiatomic Rare Earth Oxides with a Narrow Band Gap and Associated Praseodymium Multivalency. *Dalton. Trans.* **2017**, *46*, 12167–12176. [CrossRef]
9. Miracle, D.B. High Entropy Alloys as a Bold Step Forward in Alloy Development. *Nat. Commun.* **2019**, *10*, 1805. [CrossRef]
10. Miracle, D.B.; Senkov, O.N. A Critical Review of High Entropy Alloys and Related Concepts. *Acta Mater.* **2017**, *122*, 448–511. [CrossRef]
11. Liang, B.; Ai, Y.; Wang, Y.; Liu, C.; Ouyang, S.; Liu, M. Spinel-Type $(FeCoCrMnZn)_3O_4$ High-Entropy Oxide: Facile Preparation and Supercapacitor Performance. *Materials* **2020**, *13*, 5798. [CrossRef] [PubMed]
12. Baiutti, F.; Chiabrera, F.; Acosta, M.; Diercks, D.; Parfitt, D.; Santiso, J.; Wang, X.; Cavallaro, A.; Morata, A.; Wang, H.; et al. A High Entropy Manganite in an Ordered Nanocomposite for Long-Term Application in Solid Oxide Cells. *Nat. Commun.* **2021**, *12*, 2660. [CrossRef]
13. Lal, M.S.; Sundara, R. High Entropy Oxides—A Cost-Effective Catalyst for the Growth of High Yield Carbon Nanotubes and Their Energy Applications. *ACS Appl. Mater. Interfaces* **2019**, *11*, 30846–30857. [CrossRef] [PubMed]
14. Albedwawi, S.H.; AlJaberi, A.; Haidemenopoulos, G.N.; Polychronopoulou, K. High Entropy Oxides-Exploring a Paradigm of Promising Catalysts: A Review. *Mater. Des.* **2021**, *202*, 109534. [CrossRef]
15. Dominguez, L.A.; Goodall, R.; Todd, I. Prediction and Validation of Quaternary High Entropy Alloys Using Statistical Approaches. *Mater. Sci. Technol.* **2015**, *31*, 1201–1206. [CrossRef]
16. Leong, Z.; Huang, Y.; Goodall, R.; Todd, I. Electronegativity and Enthalpy of Mixing Biplots for High Entropy Alloy Solid Solution Prediction. *Mater. Chem. Phys.* **2017**, *210*, 259–268. [CrossRef]
17. Leong, Z.; Morley, N.; Goodall, R. Dilatational Strain Biplots against Enthalpy of Mixing for Predicting High-Entropy Alloys and Complex Concentrated Alloys Phase Stability. *Mater. Chem. Phys.* **2021**, *262*, 124241. [CrossRef]
18. Liang, X.; Xue, D. Electronegativity Principles in Metal Oxides Based Supercapacitors. *Nanotechnology* **2020**, *31*, 074001. [CrossRef]
19. Mulliken, R.S. A New Electroaffinity Scale; Together with Data on Valence States and on Valence Ionization Potentials and Electron Affinities. *J. Chem. Phys.* **1934**, *2*, 782. [CrossRef]
20. Allen, L.C. Electronegativity Is the Average One-Electron Energy of the Valence-Shell Electrons in Ground-State Free Atoms. *J. Am. Chem. Soc.* **1989**, *111*, 9003–9014. [CrossRef]
21. Pauling, L. The nature of the chemical bond. IV. the energy of single bonds and the relative electronegativity of atoms. *J. Am. Chem. Soc.* **1932**, *54*, 3570–3582. [CrossRef]

22. Pettifor, D.G. Theory of the Heats of Formation of Transition-Metal Alloys. *Phys. Rev. Lett.* **1978**, *42*, 846. [CrossRef]
23. Leong, Z.; Wróbel, J.S.; Dudarev, S.L.; Goodall, R.; Todd, I.; Nguyen-Manh, D. The Effect of Electronic Structure on the Phases Present in High Entropy Alloys. *Sci. Rep.* **2017**, *7*, 39803. [CrossRef]
24. Bakker, H.; Miedema, A. *Enthalpies in Alloys: Miedema's Semi-Empirical Model*; Materials Science Foundations; Trans Tech Publications Enfield, N.H.: Uetikon-Zuerich, Switzerland, 1998; ISBN 978-0-87849-783-6.
25. Takeuchi, A.; Inoue, A. Calculations of Mixing Enthalpy and Mismatch Entropy for Ternary Amorphous Alloys. *Mater. Trans. JIM* **2000**, *41*, 1372–1378. [CrossRef]
26. Takeuchi, A.; Inoue, A. Mixing Enthalpy of Liquid Phase Calculated by Miedema's Scheme and Approximated with Sub-Regular Solution Model for Assessing Forming Ability of Amorphous and Glassy Alloys. *Intermetallics* **2010**, *18*, 1779–1789. [CrossRef]
27. Takeuchi, A.; Inoue, A. Classification of Bulk Metallic Glasses by Atomic Size Difference, Heat of Mixing and Period of Constituent Elements and Its Application to Characterization of the Main Alloying Element. *Mater. Trans.* **2005**, *46*, 2817–2829. [CrossRef]
28. Calvo-Dahlborg, M.; Brown, S.G.R. Hume-Rothery for HEA Classification and Self-Organizing Map for Phases and Properties Prediction. *J. Alloys Compd.* **2017**, *724*, 353–364. [CrossRef]
29. Ghosh, D.C.; Gupta, K. A new scale of electronegativity of 54 elements of periodic table based on polarizability of atoms. *J. Theor. Comput. Chem.* **2006**, *5*, 895–911. [CrossRef]
30. Wolfram Research, Inc. *Mathematica*; 10.4; Wolfram Research, Inc.: Champaign, IL, USA, 2016.
31. Reeves-McLaren, N.; Sharp, J.; Beltrán-Mir, H.; Rainforth, W.M.; West, A.R. Spinel–Rock Salt Transformation in $LiCoMnO4_{-\delta}$. *Proc. R. Soc. A* **2016**, *472*, 20140991. [CrossRef]
32. Gao, Z.; Liu, Y.; Lu, C.; Ma, Y.; Xia, Y.; Fang, L.; He, Q.; Liu, Y.; Liu, G.; Yang, J.; et al. Origin of the Phase Change from Pyrochlore to Perovskite-like Layered Structure and a New Lead Free Ferroelectric. *arXiv* **2017**, arXiv:1703.01016.
33. Chen, Y.; Fu, H.; Huang, Y.; Huang, L.; Zheng, X.; Dai, Y.; Huang, Y.; Luo, W. Opportunities for High-Entropy Materials in Rechargeable Batteries. *ACS Mater. Lett.* **2021**, *3*, 160–170. [CrossRef]
34. Chen, H.; Qiu, N.; Wu, B.; Yang, Z.; Sun, S.; Wang, Y. A New Spinel High-Entropy Oxide $(Mg_{0.2}\ Ti_{0.2}\ Zn_{0.2}\ Cu_{0.2}\ Fe_{0.2}\ )_3\ O_4$ with Fast Reaction Kinetics and Excellent Stability as an Anode Material for Lithium Ion Batteries. *RSC Adv.* **2020**, *10*, 9736–9744. [CrossRef]
35. Wang, D.; Jiang, S.; Duan, C.; Mao, J.; Dong, Y.; Dong, K.; Wang, Z.; Luo, S.; Liu, Y.; Qi, X. Spinel-Structured High Entropy Oxide $(FeCoNiCrMn)_3O_4$ as Anode towards Superior Lithium Storage Performance. *J. Alloys Compd.* **2020**, *844*, 156158. [CrossRef]
36. Lökçü, E.; Toparli, Ç.; Anik, M. Electrochemical Performance of $(MgCoNiZn)_{1-x}\ Li_x\ O$ High-Entropy Oxides in Lithium-Ion Batteries. *ACS Appl. Mater. Interfaces* **2020**, *12*, 23860–23866. [CrossRef] [PubMed]
37. Lun, Z.; Ouyang, B.; Kwon, D.-H.; Ha, Y.; Foley, E.E.; Huang, T.-Y.; Cai, Z.; Kim, H.; Balasubramanian, M.; Sun, Y.; et al. Cation-Disordered Rocksalt-Type High-Entropy Cathodes for Li-Ion Batteries. *Nat. Mater.* **2021**, *20*, 214–221. [CrossRef]
38. Tsirelson, V.G.; Avilov, A.S.; Lepeshov, G.G.; Kulygin, A.K.; Stahn, J.; Pietsch, U.; Spence, J.C.H. Quantitative Analysis of the Electrostatic Potential in Rock-Salt Crystals Using Accurate Electron Diffraction Data. *J. Phys. Chem. B* **2001**, *105*, 5068–5074. [CrossRef]
39. Pirgholi-Givi, G.; Azizian-Kalandaragh, Y.; Farazin, J. Comparison of the Photocatalytic Activity of Perovskite Structures: Bismuth, Barium, and Zinc Titanate Nanostructures for Photodegradation of Methylene Blue from Water. *J. Photochem. Photobiol. A* **2021**, *408*, 113104. [CrossRef]